On the redistribution of charge in La 0.7 Sr 0.3 CrO 3 /La 0.7 Sr 0.3 MnO 3 multilayer thin films

As Published: 10.1063/1.5140352

Publisher: AIP Publishing

Persistent URL: https://hdl.handle.net/1721.1/135443

Version: Final published version: final published article, as it appeared in a journal, conference proceedings, or other formally published context

AIP Advances

On the redistribution of charge in $La_{0.7}Sr_{0.3}CrO_3/La_{0.7}Sr_{0.3}MnO_3$ multilayer thin films

Cite as: AIP Advances **10**, 045113 (2020); https://doi.org/10.1063/1.5140352
Submitted: 26 November 2019 . Accepted: 17 March 2020 . Published Online: 09 April 2020

Aubrey N. Penn, Sanaz Koohfar, Divine P. Kumah, and James M. LeBeau

On the redistribution of charge in $La_{0.7}Sr_{0.3}CrO_3/La_{0.7}Sr_{0.3}MnO_3$ multilayer thin films

Cite as: AIP Advances 10, 045113 (2020); doi: 10.1063/1.5140352
Submitted: 26 November 2019 • Accepted: 17 March 2020 •
Published Online: 9 April 2020

Aubrey N. Penn,[1] Sanaz Koohfar,[2] Divine P. Kumah,[2] and James M. LeBeau[3,a]

AFFILIATIONS

[1]Department of Materials Science & Engineering, North Carolina State University, Raleigh, North Carolina 27695, USA
[2]Department of Physics, North Carolina State University, Raleigh, North Carolina 27695, USA
[3]Department of Materials Science and Engineering, Massachusetts Institute of Technology, Cambridge, Massachusetts 02139, USA

[a]Author to whom correspondence should be addressed: lebeau@mit.edu

ABSTRACT

The atomic and electronic structures of $La_{0.7}Sr_{0.3}MnO_3$ (LSMO)/$La_{0.7}Sr_{0.3}CrO_3$ (LSCO) multilayer thin films are investigated using aberration corrected scanning transmission electron microscopy (STEM) imaging and spectroscopy. Atomic resolution high angle annular dark-field reveals that LSMO layers have an expanded out-of-plane lattice parameter compared to compressed LSCO layers, contrasting with x-ray diffraction measurements. The expansion is found to result from preferential oxygen vacancy formation in LSMO during STEM sample preparation as determined by electron energy-loss spectroscopy. The La/Sr atom column intensity is also found to oscillate by about 4% between the LSMO and LSCO layers, indicative of La/Sr concentration variation. Using energy-dispersive x-ray spectroscopy in combination with image simulations, we confirm the La/Sr inhomogeneity and elucidate the origin of charge redistribution within the multilayer. These results illuminate the sensitivity of the technique to subtle structural, chemical, and electronic features that can arise to compensate charge imbalances in complex oxide heterostructures.

$La_{0.7}Sr_{0.3}MnO_3$ (LSMO) has the highest Curie temperature of the manganites and is a promising candidate for applications in magnetic memory and spintronic devices.[1] Adopting the ABO_3 perovskite structure, the mixed charge A-site cations, Sr^{2+} and La^{3+}, cause the B-site Mn to exist in both 3+ and 4+ states within the structure. The average Mn charge is determined by the La/Sr ratio, and the multivalent Mn enables double-exchange that is responsible for LSMO's magnetism. In double-exchange, the Mn^{3+} e_g electron is transferred to the unoccupied Mn^{4+} orbital via oxygen.[2] Magnetism in LSMO is governed by these exchange interactions that are sensitive to the average Mn charge state and the Mn–O–Mn bonding; thus, the properties of LSMO can be tuned by engineering epitaxial strain and/or film composition.[3,4]

The application of ultra-thin LSMO films in devices has been stymied by the presence of a region of reduced magnetic character that arises near the interface, referred to as the magnetic dead layer (MDL).[3] The MDL thickness is dependent on the substrate and growth conditions. For example, in ultra-thin films (2–5 unit cells), the LSMO magnetism can be lost entirely. Strain due to lattice mismatch,[4,5] octahedral structure coupling,[6,7] and cation and oxygen off-stoichiometry due to the polar discontinuity[8–10] have been suggested as possible mechanisms that lead to MDL formation. To counteract MDL formation, spacer layers have been introduced between the LSMO film and the substrate in order to mitigate the interfacial impact on LSMO magnetic properties. These heterostructured materials are additionally of scientific and technological interest due to the coupling of the structure and properties when ultra-thin layers are brought into contact.

A number of spacer materials have been investigated in LSMO-based heterostructures. For example, $La_{0.5}Sr_{0.5}TiO_3$ has been

investigated for its ability to inhibit the charge transfer by introducing a Mn/Ti charge mismatch due to the varying La/Sr ratio between Mn- and Ti-containing layers.[11] In a further study, the LSMO saturation magnetization, Curie temperature, and coercivity were found to be controlled by a tetragonal distortion and interfacial dislocations when the same heterostructure was grown on substrates that induce various strain states.[12] In addition, the layer ordering of $La_{0.7}Sr_{0.3}CoO_3$–LSMO multilayer heterostructures is found to impact the charge transfer, octahedral structure, and the resulting magnetic properties of the films by changing the structural compensation mechanisms at the substrate interface.[13] Koohfar *et al.* recently reported that the architecture of the $La_{0.7}Sr_{0.3}CrO_3$ (LSCO)–LSMO heterostructure causes LSMO to retain its magnetic character when grown with a thickness of only 2 unit cells. Isovalent LSCO spacer layers not only remove the polar discontinuity at the LSMO interface and are closely lattice matched with bulk LSMO (a_{LSMO} = 3.879 Å,[14] a_{LSCO} = 3.88 Å[15]) but also reduce the octahedral structure distortion leading to LSMO films with magnetic properties comparable to bulk.[16]

Throughout prior work, scanning transmission electron microscopy (STEM) and electron energy-loss spectroscopy (EELS) have proven critical to examine structures and cation charge states in thin films. For EELS, fine spectral features from the cation and oxygen edges, energy onset, and intensity ratio of the core-loss edges are used to quantify B-site charge states and determine the film stoichiometry.[17–23] Evidence has not been provided, however, of the La/Sr stoichiometry through the film depth. Furthermore, direct comparisons between x-ray diffraction (XRD) studies and structural measurements with STEM are not often reported.

In this paper, we investigate a LSMO/LSCO multilayered heterostructure grown on $SrTiO_3$ (STO). Using high angle annular dark field (HAADF) STEM imaging and simulation, EELS, and energy dispersive x-ray spectroscopy (EDS), we show the correlation of atomic and electronic structures and film chemistry. We find an inhomogeneous La/Sr ratio that differs between LSMO and LSCO, which is observed in HAADF STEM images and EDS. Furthermore, EELS analysis indicates that there is preferential oxygen vacancy formation in LSMO layers accompanied by an out-of-plane lattice expansion. These results are compared with XRD studies to highlight the need to combine the measurements from multiple modalities to fully capture the details of charge redistribution.

LSMO/LSCO heterostructures were grown using molecular beam epitaxy (MBE). *In situ* reflection high energy electron diffraction was used to control the thickness of the layers with atomic-layer precision. LSCO and LSMO layers were grown at 900 °C in an oxygen plasma pressure of 10^{-6} Torr on (001) oriented STO with TiO_2 surface termination. Prior to growth, the atomic fluxes were calibrated with a quartz crystal monitor to within 5%–10% of the desired rates. The heterostructures were slowly cooled to room temperature after growth in the same oxygen plasma pressure to ensure that the samples are fully oxidized. The heterostructure grown was 2 unit cells of LSCO and 3 unit cells of LSMO, repeated eight times producing a 40 unit cell thick film. This structure is denoted as [3 LSMO/2 LSCO] × 8.

Samples for electron microscopy were prepared by mechanical polishing and single-sector ion milling[24] at intervals of decreasing voltage beginning at 2 kV and finishing at 0.5 kV. A probe-corrected FEI Titan G2 80-300 kV scanning transmission electron microscope was operated at 200 kV for STEM imaging and EELS. HAADF STEM images were collected using the Revolving STEM (RevSTEM) method to maximize the signal to noise ratio and minimize the effects of drift and scan distortion.[25] Accurate and precise atom column positions were determined from RevSTEM images using custom MATLAB programs that are available upon request.[26] STEM images were simulated using the multislice method.[27] Atom column intensity measurements were performed using a Voronoi partitioned integration window to minimize the influence of microscope aberrations.[28] EEL spectra were acquired with a Gatan Enfinium Spectrometer (40 mrad collection angle), with an energy resolution of 0.35 eV and a dispersion of 0.05 eV/channel. The probe current was 100 pA. The Mn charge state was determined using non-linear least squares fitting to MnO, Mn_2O_3, and MnO_2 reference spectra. EDS was performed for elemental concentration measurements with Super-X detectors and 80 pA beam current. EDS line profiles were formed by averaging the concentration values from 2D maps. Detailed information of simulations, EELS data processing and quantification, and EDS maps can be found in the supplementary material.

To determine the lattice constants of the LSMO and LSCO layers of the as-grown samples, crystal truncation rods (CTRs) were measured on a [2 LSMO/2 LSCO] × 10 sample at the 33ID beamline at the Advanced Photon Source. Figure 1 shows measured diffraction data around the (112) Bragg peak. Finite thickness oscillations and superlattice peaks observed are indicative of the crystalline quality and periodicity of the superlattice. The lattice constants of the LSCO and LSMO layers are varied to fit the measured data. The measured and simulated CTRs for the sample are compared in Fig. 1, and the figure shows good agreement between them.

HAADF STEM reveals that the [3 LSMO/2 LSCO] × 8 heterostructure is free of interfacial defects, as shown in Fig. 2(a).

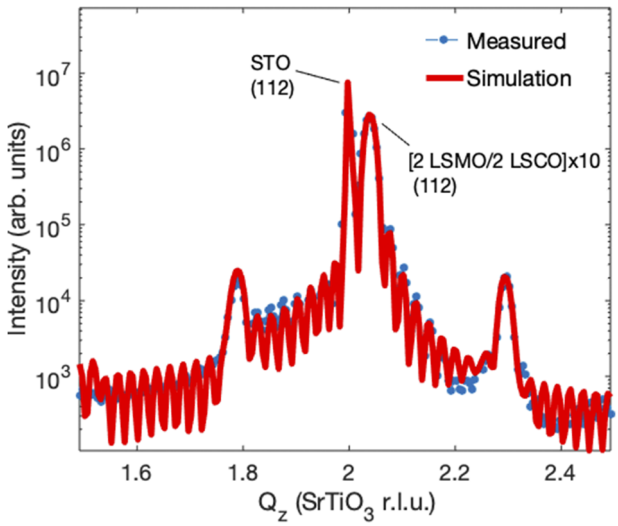

FIG. 1. Crystal truncation rod measurement around the (112) film and the substrate Bragg peak for a [2 LSMO/2 LSCO] × 10 superlattice grown on STO. The simulation is determined from a fit to the experimentally measured diffraction intensities.

The HAADF scales roughly as $Z^{1.6}$, where Z is the atomic number (Z_{Cr} = 24, Z_{Mn} = 25) supplementary material. As such, simulations indicate that the Mn atom columns are expected to exhibit 5.8% greater intensity than Cr [supplementary material Fig. S1(c)]. As measured from HAADF STEM in Fig. 2(b), the average difference of the Cr/Mn atom columns in the LSCO and LSMO is 3.2%, which is significantly less than expected. Furthermore, La/Sr (Z_{La} = 52, Z_{Sr} = 38) atom column intensities are expected to be constant across the heterostructure if the La to Sr ratio is also constant. However, the intensity of the La/Sr atom columns shown in Fig. 2(b) indicates that these atom columns are periodically 3.7% brighter in the nominal LSMO layers.

To understand the compositional variations observed by the HAADF, atomic layer resolved EELS was performed. Figure 2(c) shows the maps of the integrated Cr/Mn L-edge intensity. Comparing with the HAADF intensity profiles in Fig. 2(b), it is revealed that the brightest La/Sr atom columns occur in the LSMO layers. Figure 2(d) presents the Mn/Cr composition profiles measured from the integrated intensity of Mn and Cr L-edges in Fig. 2(c) revealing intermixing. This degree of chemical intermixing explains the discrepancy in the intensity of nominal Mn- and Cr-containing atom columns between experimental and simulated images. Although the observed intermixing in EELS can be due to beam broadening through the thickness of the sample,[30] STEM probe simulations indicate that beam spreading is limited to about 0.05 nm for the 9 nm thick TEM sample.

Compositional analysis of these layers by EDS, shown in Fig. 2(e), also indicates that the Sr signal increases by 2 ± 0.2 at. % in the LSCO layers compared to LSMO, which is in agreement with the decreased HAADF intensity in these regions. To validate the subtle EDS observations, STEM image simulations were performed with a 60/40 La/Sr ratio in LSCO compared to the nominal 70/30 ratio in LSMO. The adjusted ratio was chosen based on the sensitivity of the Mn charge state calculations discussed later. The average La/Sr column intensity of the layers from the image simulations [supplementary material Fig. S1(c)] shows a 5% decrease in LSCO, where the Sr concentration is greater. Therefore, the change in the La/Sr ratio can readily account for the 3.7% variation in the atom column intensity in experimental images. This change in the composition across the multilayer stack can have at least two main impacts. First, the structure (lattice parameter and octahedral structure) would be modified based on the ratio of the La/Sr atom columns. Second, the charge state of Mn or Cr can change to account for the change in the atomic layer-averaged A-site charge. While changes in both HAADF and EDS signals are small, the measured values are above the sensitivity limits for both techniques. A sensitivity of 0.1% is standard for the Super-X EDS detectors with sufficient counts.[31] Furthermore, the EDS peaks considered for quantification do not overlap; therefore, the changing B-site chemistry does not affect La/Sr quantification. Furthermore, the HAADF can be sensitive to ±1 atom in an atom column when accompanied by simulation.[32]

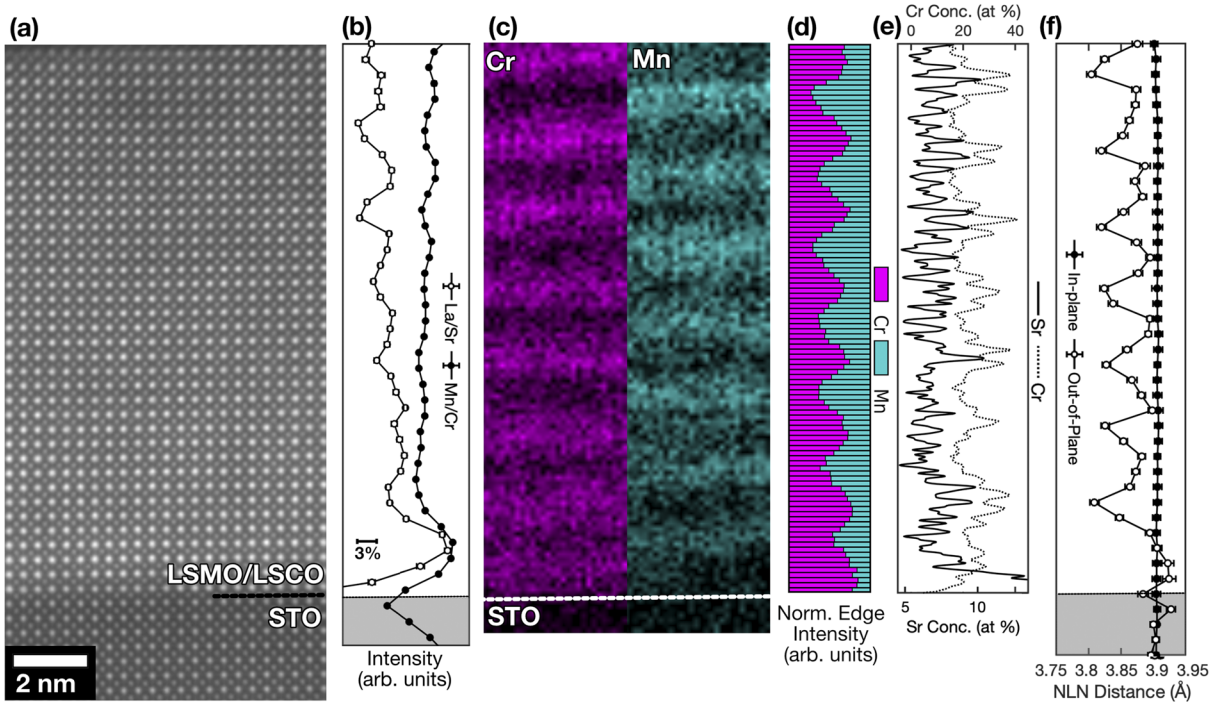

FIG. 2. (a) HAADF RevSTEM image of the [3 LSMO/2 LSCO] × 8 heterostructure on STO. (b) Intensity profiles of La/Sr and Mn/Cr atom columns. (c) Cr and Mn EELS maps with composition profiles (d) of Mn and Cr EELS L-edges showing intermixing. (e) Atomically resolved Sr and Cr concentrations from EDS. (f) In- and out-of-plane nearest-like neighbor (NLN) distances. The substrate region is marked with a gray box.

To determine structural changes, the in- and out-of-plane nearest-like neighbor (NLN) atom column distances are determined using atom column positions in HAADF STEM images and XRD. Figure 2(f) shows the STEM-determined average in-plane measurement of 3.905 Å, revealing that the film is pseudomorphic to STO, in agreement with the XRD results.[16] Because the film is tensile strained in-plane, the out-of-plane parameter is expected to compress.

Figure 1 shows the off-specular (11*L*) crystal truncation rod for the [2 LSMO/2 LSCO] × 10 sample on STO. Clear superlattice peaks are observed indicative of distinct LSCO and LSMO layers and rules out the formation of a solid solution of (LaSr) (CrMn)O_3. By fitting the measured diffraction data using GenX,[33] the out-of-plane lattice constants are determined for the LSCO and LSMO layers to be 3.821 ± 0.005 Å and 3.846 ± 0.005 Å, respectively. A similar analysis for the [6 LSMO/2 LSCO] × 4 sample yields identical lattice parameters, confirming that increasing the LSMO thickness does not lead to the relaxation of strain in the LSCO and LSMO layers. The oscillatory out-of-plane parameter is captured in the STEM-determined NLN distance in Fig. 2(f). The average LSCO parameter is 3.81 ± 0.01 Å, in agreement with XRD. LSMO layers, however, exhibit an average out-of-plane parameter of 3.88 ± 0.01 Å, approximately 4 pm larger than that of the XRD-determined value.

The valence state of Mn across the multilayer is determined by fitting the EELS L_3 and L_2 white lines to Mn^{2+}, Mn^{3+}, and Mn^{4+} references using non-linear least squares fitting.[9] An average Mn charge of 3.4 ± 1 is nearly constant throughout the film, as shown in Fig. 3(a). There is no clear charge oscillation within each layer, thus suggesting that the charge transfer between the layers does not occur. It is worth noting here that the reference and experimental spectra were aligned by the L_3 edge onset so that only the edge shapes were considered as parameters in the fitting as shown in supplementary material Fig. S2. This fitting constraint was chosen due to an observed periodic shifting of the Mn L_3 edge, with each layer of the heterostructure, as shown in Fig. 3(b). An example of the Mn L-edge in LSMO compared to intermixed Mn in nominal LSCO layers is shown in Fig. 3(c). Dashed vertical lines show the 0.5 eV shift between the two edges. The onset of the Mn L_3 edge reaches a maximum of 645.8 eV in LSMO layers and decreases to 645.3 eV in nominal LSCO layers. This edge shifting can be indicative of varying charge states,[17] but this does not agree with the charge determined from references.

To explain the edge shifts observed in EELS data, the O K-edge extended loss near-edge structure is examined. The O K-edge pre-peak at 533 eV is due to Mn/Cr–O hybridization and is reduced when oxygen vacancies are present or shifts with a change in Mn valence.[18,21,34] Figure 3(d) shows that the O pre-peak occurs in LSCO layers but is diminished in LSMO. This strongly suggests that oxygen vacancies accumulate in LSMO layers.

Cr charge state determination with EELS has proven complicated in bulk materials and is further complicated by the strain, lattice distortions, and complex chemistry of the film studied here.[35] The most reliable approach is to measure the distance between the O K-edge pre-peak and the Cr L_3 edge.[36] In LSMO layers where Cr has intermixed, the pre-peak is not present or lost in the noise, so such an analysis is not possible with Cr. While charge state analysis is not possible on both Mn and Cr, the claim here that there is no charge transfer between Mn and Cr is corroborated in previous work on this heterostructure.[16]

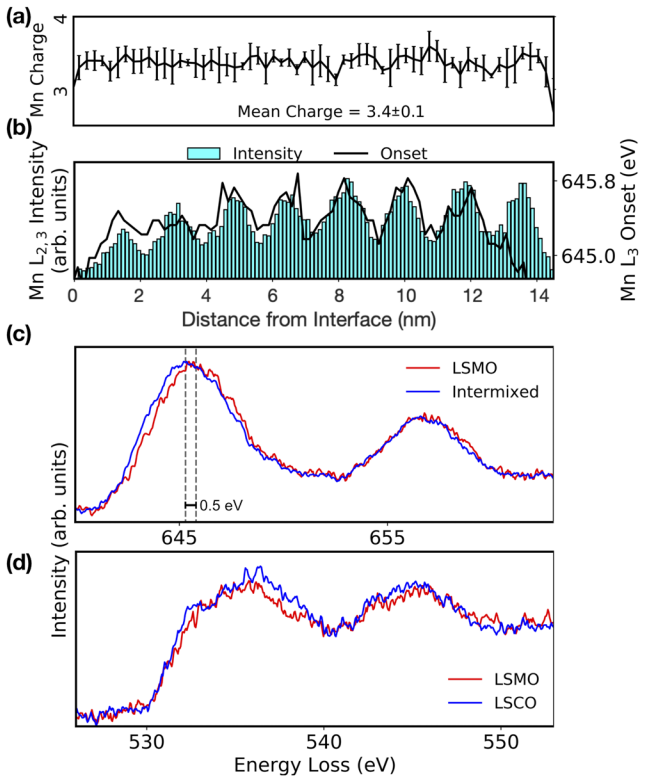

FIG. 3. (a) Layer-resolved Mn charge states determined from fits to EELS spectra. The error bar is the standard error of the depth-dependent charge state using 3 Mn EELS line scans. (b) Mn L_3-edge shifts through the film thickness overlaying the integrated intensity of the Mn L_3-edge. (c) Representative Mn L-edge taken from LSMO compared to intermixed Mn from nominal LSCO layers. The vertical dashed lines indicate the 0.5 eV shift between the edges. (d) Comparison of oxygen K-edge from LSMO and LSCO layers.

The preferential formation of $La_{0.7}Sr_{0.3}MnO_{3-\delta}$ oxygen vacancies explains the observed expanded out-of-plane lattice parameter in these layers. The oxygen vacancies cause nearby cation repulsion, subsequently expanding the lattice. The degree of lattice expansion corresponds to an approximate oxygen deficiency of $\delta = 0.125$, or approximately one vacancy for every 8 unit cells.[37] Since the film remains pseudomorphic to STO, only the out-of-plane parameter increases. The oxygen vacancy-induced expansion also explains the oscillating Mn EELS L_3-edge onsets observed in Fig. 3(b). Although the edge onset shift can be indicative of the charge transfer between Mn and Cr,[13] oxygen vacancies would also reduce the Mn charge. Mn appears, however, to maintain its valence based on the reference fits. If any change in the Mn charge occurs, it is within the precision of the measurement, ± 0.1 eV. Rather, the phenomenon is most likely the result of tetragonal distortion increasing the energy split of Mn *t2g* and *eg* orbitals, consistent with the results from $SrMnO_3$ thin films grown with different strain states.[34]

The presence of positively charged oxygen vacancy point defects ($V_O^{\bullet\bullet}$, using Kröger–Vink Notation) in LSMO layers without a Mn charge decrease indicates that the charge compensation mechanism occurs in the La/Sr cation sublattice. The reduced La/Sr

atom column intensity in LSCO is due to either of the two possible phenomena: Sr excess in LSCO (as was simulated) or negatively charged Sr vacancies (V''_{Sr}) in LSMO to balance $V^{\bullet\bullet}_{O}$. From the simulated intensity calculations, the 3.7% change in the La/Sr column intensity is due to less than a 10% V''_{Sr} or the La/Sr ratio change in the layers, which is below the sensitivity of the EELS-determined Mn charge measurement.

The non-uniform La/Sr ratio is consistent with interdiffusion on the order of a unit cell observed at complex oxide interfaces and may be kinetically driven by intermixing resulting from the high growth temperature (800 °C) required to achieve epitaxial growth.[38–40]

The EELS results also explain the discrepancy between the LSMO out-of-plane lattice parameter from XRD and STEM measurements. The STEM measured value of 3.88 Å is 4 pm greater than the XRD value of 3.84 Å, consistent with the values for LSMO grown by MBE on STO under oxygen deficient and stoichiometric conditions, respectively.[37] Furthermore, the lattice parameter for LSCO layers for both XRD and STEM is in good agreement, and thus, the discrepancy is not due to the systematic measurement error in either method. The observed mismatch can thus be explained by the formation of oxygen vacancies in LSMO during TEM sample preparation, resulting in the decrease of the O K-edge pre-peak intensity and the increased out-of-plane lattice parameter. During preparation for TEM, the top and bottom sample surfaces perpendicular to the electron beam are exposed. While LSMO and LSCO layers are equally exposed to the preparation process, both the differing B-site chemistry and the varied La/Sr ratio can easily reduce the oxygen vacancy formation energy, allowing a higher concentration of vacancies to form in LSMO. Small changes in doping, for example, have shown to change this value by several electron volts.[41] We confirm that the lattice expansion is independent of the electron dose during imaging, indicating that the effect is already present in the as-prepared samples for electron microscopy. Further investigation of the sample preparation steps responsible for oxygen vacancy formation is required, and additional post-TEM preparation steps are likely needed to fully probe the underlying mechanism.

In conclusion, we have characterized the structure and chemistry of an MBE-grown LSMO–LSCO multilayer heterostructure using STEM imaging, simulation, EDS, and EELS. The La/Sr ratio, oxygen stoichiometry, and resultant lattice parameter were found to vary with each layer. These results strongly suggest that it is critical to examine the energy-loss edge onsets, the fine structure of cation and oxygen edges, and the La/Sr chemical heterogeneity in determining multilayer valence. Oxygen vacancies are found to preferentially form in the LSMO layers during TEM sample preparation. These results indicate that acquiring a combination of precise and accurate structural data with EELS is essential to fully explain the observed trends in either technique.

See the supplementary material for information on EELS data processing and quantification, STEM image simulations, and expanded STEM EDS maps.

A.N.P. and J.M.L. acknowledge support from the National Science Foundation under Grant No. DMR-1350273. S.K. and D.P.K. acknowledge financial support from the U.S. National Science Foundation under Grant No. NSF DMR-1751455. This work was performed in part at the Analytical Instrumentation Facility (AIF) at North Carolina State University, which was supported by the State of North Carolina and the National Science Foundation (Award No. ECCS-1542015). This work made use of instrumentation at AIF acquired with support from the National Science Foundation (Grant No. DMR-1726294). The AIF is a member of the North Carolina Research Triangle Nanotechnology Network (RTNN), a site in the National Nanotechnology Coordinated Infrastructure (NNCI). Use of the Advanced Photon Source was supported by the U.S. Department of Energy, Office of Science, Office of Basic Energy Sciences, under Contract No. DE-AC02-06CH11357.

REFERENCES

[1] Z. H. Xiong, D. Wu, Z. Valy Vardeny, and J. Shi, Nature **427**, 821 (2004).
[2] C. Zener, Phys. Rev. **82**, 403 (1951).
[3] W. Guichard, J. G. Lunney, J. M. D. Coey, F. Ott, and R. P. Borges, J. Appl. Phys. **89**, 3868 (2002).
[4] M. Nord, P. E. Vullum, M. Moreau, J. E. Boschker, S. M. Selbach, R. Holmestad, and T. Tybell, Appl. Phys. Lett. **106**, 041604 (2015).
[5] A. Vailionis, H. Boschker, Z. Liao, J. R. A. Smit, G. Rijnders, M. Huijben, and G. Koster, Appl. Phys. Lett. **105**, 131906 (2014).
[6] M. Huijben, G. Koster, Z. L. Liao, and G. Rijnders, Appl. Phys. Rev. **4**, 041103 (2017).
[7] Z. Liao, M. Huijben, Z. Zhong, N. Gauquelin, S. Macke, R. J. Green, S. Van Aert, J. Verbeeck, G. Van Tendeloo, K. Held, G. A. Sawatzky, G. Koster, and G. Rijnders, Nat. Mater. **15**, 425 (2016).
[8] N. Nakagawa, H. Y. Hwang, and D. A. Muller, Nat. Mater. **5**, 204 (2006).
[9] J. A. Mundy, Y. Hikita, T. Hidaka, T. Yajima, T. Higuchi, H. Y. Hwang, D. A. Muller, and L. F. Kourkoutis, Nat. Commun. **5**, 3464 (2014).
[10] R. Trappen, A. C. Garcia-Castro, V. T. Tra, C. Y. Huang, W. Ibarra-Hernandez, J. Fitch, S. Singh, J. Zhou, G. Cabrera, Y. H. Chu, J. M. LeBeau, A. H. Romero, and M. B. Holcomb, Sci. Rep. **8**, 1 (2018).
[11] F. Yang, M. Gu, E. Arenholz, N. D. Browning, and Y. Takamura, J. Appl. Phys. **111**, 013911 (2012).
[12] M. Gu, C. Song, F. Yang, E. Arenholz, N. D. Browning, and Y. Takamura, J. Appl. Phys. **111**, 084906 (2012).
[13] J. P. Byers, B. Li, R. V. Chopdekar, J. Ditto, D. C. Johnson, Y. Takamura, and N. D. Browning, J. Appl. Phys. **125**, 082518 (2019).
[14] P. G. Radaelli, G. Iannone, M. Marezio, H. Y. Hwang, S.-W. Cheong, J. D. Jorgensen, and D. N. Argyriou, "Structural effects on the magnetic and transport properties of perovskite $A_{1-x}A'_xMnO_3$ (x = 0.25, 0.30)," Phys. Rev. B **56**(13), 8265–8276(1997).
[15] K. Tezuka, Y. Hinatsu, A. Nakamura, T. Inami, Y. Shimojo, and Y. Morii, J. Solid State Chem. **141**, 404 (1998).
[16] S. Koohfar, A. B. Georgescu, A. N. Penn, J. M. LeBeau, E. Arenholz, and D. P. Kumah, npj Quantum Mater. **4**, 25 (2019).
[17] H. Tan, J. Verbeeck, A. Abakumov, and G. Van Tendeloo, Ultramicroscopy **116**, 24 (2012).
[18] M. Varela, M. P. Oxley, W. Luo, J. Tao, M. Watanabe, A. R. Lupini, S. T. Pantelides, and S. J. Pennycook, Phys. Rev. B **79**, 085117 (2009).
[19] H. Kurata and C. Colliex, Phys. Rev. B **48**, 2102 (1993).
[20] Z. L. Wang, J. S. Yin, Y. D. Jiang, and J. Zhang, Appl. Phys. Lett. **70**, 3362 (1997).
[21] Z. Li, M. Bosman, Z. Yang, P. Ren, L. Wang, L. Cao, X. Yu, C. Ke, M. B. H. Breese, A. Rusydi, W. Zhu, Z. Dong, and Y. L. Foo, Adv. Funct. Mater. **22**, 4312 (2012).
[22] O. L. Krivanek, M. M. Disko, J. Taftø, and J. C. H. Spence, Ultramicroscopy **9**, 249 (1982).
[23] L. F. Kourkoutis, J. H. Song, H. Y. Hwang, and D. A. Muller, Proc. Natl. Acad. Sci. U. S. A. **107**, 11682 (2010).
[24] L. Dieterle, B. Butz, and E. Müller, Ultramicroscopy **111**, 1636 (2011).
[25] X. Sang and J. M. LeBeau, Ultramicroscopy **138**, 28 (2014).
[26] X. Sang, A. A. Oni, and J. M. LeBeau, Microsc. Microanal. **20**, 1764 (2014).

[27]E. J. Kirkland, *Advanced Computing in Electron Microscopy* (Springer, 2013).
[28]H. E, K. E. MacArthur, T. J. Pennycook, E. Okunishi, A. J. D'Alfonso, N. R. Lugg, L. J. Allen, and P. D. Nellist, Ultramicroscopy **133**, 109 (2013).
[29]O. L. Krivanek, M. F. Chisholm, V. Nicolosi, T. J. Pennycook, G. J. Corbin, N. Dellby, M. F. Murfitt, C. S. Own, Z. S. Szilagyi, M. P. Oxley, S. T. Pantelides, and S. J. Pennycook, Nature **464**, 571 (2010).
[30]R. F. Egerton, Ultramicroscopy **107**, 575 (2007).
[31]H. S. Von Harrach, P. Dona, B. Freitag, H. Soltau, A. Niculae, and M. Rohde, Microsc. Microanal. **15**, 208 (2009).
[32]J. M. Lebeau, S. D. Findlay, L. J. Allen, and S. Stemmer, Nano Lett. **10**, 4405 (2010).
[33]M. Björck and G. Andersson, J. Appl. Crystallogr. **40**, 1174 (2007).
[34]P. Agrawal, J. Guo, P. Yu, C. Hébert, D. Passerone, R. Erni, and M. D. Rossell, Phys. Rev. B **94**, 104101 (2016).
[35]T. L. Daulton and B. J. Little, Ultramicroscopy **106**, 561 (2006).
[36]Á. M. Arévalo-López and M. Á. Alario-Franco, Inorg. Chem. **48**, 11843 (2009).
[37]P. Orgiani, A. Y. Petrov, R. Ciancio, A. Galdi, L. Maritato, and B. A. Davidson, Appl. Phys. Lett. **100**, 042404 (2012).
[38]A. Gozar, G. Logvenov, L. F. Kourkoutis, A. T. Bollinger, L. A. Giannuzzi, D. A. Muller, and I. Bozovic, Nature **455**, 782 (2008).
[39]S. A. Chambers, M. H. Engelhard, V. Shutthanandan, Z. Zhu, T. C. Droubay, L. Qiao, P. Sushko, T. Feng, H. D. Lee, T. Gustafsson *et al.*, Surf. Sci. Rep. **65**, 317 (2010).
[40]M. Waschk, A. Sarkar, J. Barthel, J. Voigt, S. Schröder, P. Zakalek, M. Schmitz, B. Kirby, S. Pütter, J. Schubert *et al.*, J. Phys.: Condens. Matter **32**, 11 (2020).
[41]T. Ishihara, *Perovskite Oxide for Solid Oxide Fuel Cells,* Fuel Cells and Hydrogen Energy (Springer, 2009), p. 310.